

Numerical Heat Transfer, Part B: Fundamentals

An International Journal of Computation and Methodology

ISSN: 1040-7790 (Print) 1521-0626 (Online) Journal homepage: <http://www.tandfonline.com/loi/unhb20>

A Finite-Volume Model for Fluid Flow and Nonequilibrium Heat Transfer in Conjugate Fluid-Porous Domains Using General Unstructured Grids

Christopher T. DeGroot & Anthony G. Straatman

To cite this article: Christopher T. DeGroot & Anthony G. Straatman (2011) A Finite-Volume Model for Fluid Flow and Nonequilibrium Heat Transfer in Conjugate Fluid-Porous Domains Using General Unstructured Grids, Numerical Heat Transfer, Part B: Fundamentals, 60:4, 252-277, DOI: [10.1080/10407790.2011.601180](https://doi.org/10.1080/10407790.2011.601180)

To link to this article: <http://dx.doi.org/10.1080/10407790.2011.601180>



Published online: 14 Sep 2011.



Submit your article to this journal [↗](#)



Article views: 306



View related articles [↗](#)



Citing articles: 10 View citing articles [↗](#)

A FINITE-VOLUME MODEL FOR FLUID FLOW AND NONEQUILIBRIUM HEAT TRANSFER IN CONJUGATE FLUID-POROUS DOMAINS USING GENERAL UNSTRUCTURED GRIDS

Christopher T. DeGroot and Anthony G. Straatman

Department of Mechanical and Materials Engineering, The University of Western Ontario, London, Ontario, Canada

A numerical model for computing fluid flow and heat transfer, under the assumption of local thermal nonequilibrium, is proposed for use with general unstructured, nonorthogonal grids. This model introduces novel interface conditions which are physically-reasoned and ensure strong coupling between the pressure and velocity fields. Special attention is given to the numerical approximation of diffusive and advective fluxes, pressure forces in the momentum equations, pressure-velocity coupling, and gradient reconstruction at interfaces while maintaining second-order accuracy. The resulting model is very robust and is shown to produce physically reasonable results for high laminar Reynolds numbers on nonorthogonal grids.

1. INTRODUCTION

Problems involving fluid flow and heat transfer in domains containing both fluid and porous regions have many applications in areas such as filtration, packed-bed reactors, and thermal management. In recent years there has been significant interest in the use of high-porosity, high-conductivity metallic foams for heat transfer enhancement [1–8]. In order to effectively simulate the performance of such devices, there is a need to develop robust mathematical and numerical models, which are capable of accurately computing the flow and thermal fields in fluid and porous regions as well as maintaining coupling at interfaces between these regions. While the equations governing heat and fluid flow in porous media are readily derived using the method of volume averaging [9] in conjunction with suitable closure models such as the empirically based models of Vafai and Tien [10], it often remains challenging to obtain physically reasonable solutions in the vicinity of fluid-porous interfaces.

Received 4 April 2011; accepted 9 June 2011.

The authors wish to acknowledge the financial support provided by the Natural Sciences and Engineering Research Council (NSERC) and the computing facilities provided by the Shared Hierarchical Academic Research Computing Network (SHARCNET: www.sharcnet.ca) and Compute/Calcul Canada.

Address correspondence to Christopher T. DeGroot, Department of Mechanical and Materials Engineering, The University of Western Ontario, London, ON N6A 5B9, Canada. E-mail: cdegroot@uwo.ca

NOMENCLATURE

a	active coefficient in discretized equation	\mathbf{x}	position vector ($= [x, y, z]$), m
a_{fs}	specific surface area of porous medium, m^{-1}	$\langle \rangle$	denotes extrinsic volume average
A	area, m^2	$\langle \rangle^k$	denotes intrinsic volume average with respect to constituent $k \in \{f, s\}$
b	source term in discretized equation	Greek Symbols	
c	specific heat capacity for a solid, J/kg K	Γ	diffusion coefficient
c_f	form drag coefficient for porous medium	δ	characteristic grid spacing or a small distance
c_p	constant-pressure specific heat capacity, J/kg K	δ_{ij}	Kronecker delta tensor ($\delta_{ij} = 1$ if $i = j$, $\delta_{ij} = 0$ if $i \neq j$)
\hat{d}_{ip}	damping factor in advecting velocity equation	ε	porosity ($= V_f/V$)
$\mathbf{D}_{f,ip}$	displacement vector from $\mathbf{x}_P + f_{ip}\mathbf{D}_{P,nb}$ to \mathbf{x}_{ip} , m	μ	dynamic viscosity, kg/m s
$\mathbf{D}_{P,ip}$	displacement vector from P to ip , m	ρ	density, kg/m^3
$\mathbf{D}_{nb,ip}$	displacement vector from nb to ip , m	σ_{ij}	stress tensor, Pa
$\mathbf{D}_{P,nb}$	displacement vector from P to nb , m	ϕ	generic scalar quantity
Da	Darcy number based on channel height ($= K/H^2$)	Ω	denotes a three-dimensional space
f_{ip}	parameter for inverse distance interpolations	$\partial\Omega$	denotes a surface bounding a space Ω
h_{fs}	interfacial heat transfer coefficient, $\text{W/m}^2 \text{K}$	Subscripts and Superscripts	
H	channel height, m	f	fluid
k	thermal conductivity, W/m K	fe	effective fluid property in porous region
K	permeability of porous medium, m^2	fl	quantity associated with the fluid region
\dot{m}	mass flux, kg/s	in	inlet
\mathbf{n}	unit-normal vector	ip	quantity evaluated at or associated with an integration point
N_{ip}	number of discrete control surfaces on $\partial\Omega_P$	nb	quantity evaluated at or associated with a neighboring control volume
p	pressure, Pa	P	quantity evaluated at or associated with a particular control volume
q''	heat flux, W/m^2	por	quantity associated with the porous region
Re_H	Reynolds number based on channel height ($= \rho_f UH/\mu_f$)	s	solid
t	time, s	se	effective solid property in porous region
T	temperature, K	w	wall
\mathbf{u}	fluid velocity vector ($= [u, v, w]$), m/s	$+$	approaching from the nb side of an interface
$\hat{\mathbf{u}}$	advecting velocity, m/s	$-$	approaching from the P side of an interface
$\tilde{\mathbf{u}}$	pseudo-velocity, m/s		
V	volume, m^3		

Several different numerical models have been proposed for the simulation of flow and heat transfer in conjugate domains using staggered, orthogonal finite-volume grids, under the assumption of either local thermal equilibrium [11–13] or nonequilibrium [14]. While equilibrium models are appropriate where the fluid and solid conductivities are similar, it is necessary to consider local thermal non-equilibrium and solve separate, coupled energy equations for each constituent when the conductivities are substantially different as in many heat transfer applications

[14, 15]. As a result, Phanikumar and Mahajan [14] extended the applicability of earlier conjugate models by considering local thermal nonequilibrium between the fluid and solid constituents. While all of these algorithms were successful for their specific applications, which were two-dimensional and easily discretized using orthogonal grids, it is quite challenging to implement a staggered grid formulation for more general three-dimensional problems where nonorthogonal grids are required.

More recently there have been models proposed which utilize collocated grids, where the grids used for pressure and velocity calculations are identical. For example, Costa et al. [16, 17] proposed a control-volume finite-element model for conjugate domains that was developed generally for arbitrary unstructured grids; however, the model was only tested for relatively simple geometries that were discretized using orthogonal grids. Thus, it is unclear how the model would perform for nonorthogonal grids. Betchen et al. [18] proposed a collocated finite-volume model and introduced an improved estimate of the interface pressure, which allowed results to be obtained at high Reynolds numbers for interfaces perpendicular to the flow direction. As described in this work, it is much more challenging to obtain physically reasonable solutions in the neighborhood of a porous-fluid interface when the flow is perpendicular to that interface as a result of the change in the form of the advected momentum flux across the interface. At high flow rates, this results in a significant change in pressure in the immediate vicinity of the interface in order to satisfy a momentum balance on the fluid side of the interface [18]. This effect is most pronounced for internal flows where the fluid is forced to pass through the porous medium, as opposed to external flows where much of the fluid flows around the porous region.

The idea of a pressure correction at interfaces has not been well studied in the literature, due in part to the fact that many previous studies have focused on low-Reynolds-number flows where the change in pressure as a result of the change in the advected velocity is indeed negligible. Additionally, there have been several models proposed [11, 12, 16] which use an advected velocity in the porous region that is a factor of ε too large, which artificially eliminates this problem even at higher Reynolds numbers. It is clear that high-Reynolds-number flows in porous media are of great practical importance in heat transfer applications, so it is important that accurate results be obtained in the presence of fluid-porous interfaces. The pressure condition proposed by Betchen et al. [18], which takes into account the rapid change in pressure resulting from the change in the advected velocity at the interface, is capable of obtaining results for high Reynolds numbers without spurious oscillations in the pressure or velocity fields. Costa et al. [17] have also reported some simulations with perpendicular interfaces at moderate Reynolds numbers; however, there still appear to be issues with spurious oscillations in pressure at the interface (as seen in Figure 9c of [17]), which is likely due to a force imbalance as a result of the change in the advected velocity across the interface without an appropriate change in pressure.

The main disadvantage of the model of Betchen et al. [18] is that it has been developed specifically for geometries which can be discretized using orthogonal grids. Yu et al. [19] implemented the interface pressure condition proposed by Betchen et al. [18] into their model, which uses multiblock, body-fitted meshes; however, their model cannot produce smooth solutions for Reynolds numbers as high as those considered by Betchen et al. [18]. This difference could stem from a multitude of factors, including the gradient reconstruction at the interface or the treatment of

the advecting and advected velocities at the interface, which are not described in detail in [19]. In any case, these results highlight the special difficulties encountered with nonorthogonal grids that must be dealt with in order to have a robust model.

In summary, it is clear that the model proposed by Betchen et al. [18] is very robust and is able to produce physically reasonable solutions for all Reynolds and Darcy numbers considered; however, some difficulties are encountered when extending the model for use on nonorthogonal grids [19]. While the model of Costa et al. [16, 17] was developed for general unstructured grids, it thus far remains largely untested for nonorthogonal grids. Additionally, even with orthogonal grids, the model of Costa et al. [16, 17] seems to produce some small unphysical oscillations in the solution fields near interfaces. Thus, the goal of this work is to develop a robust, finite-volume-based algorithm for computing conjugate fluid-porous flows, using general unstructured, nonorthogonal grids, that is able to obtain smooth solutions for all Reynolds numbers in the laminar regime.

In this article, we first outline the relevant governing equations in the fluid region and briefly outline the volume-averaging procedure that is used to derive the governing equations for the porous region. This is followed by a discussion of the interface conditions imposed at the intersection of the fluid and porous subdomains. Subsequently, the discretization of the governing equations and interface conditions and their implementation into a finite-volume computational fluid dynamics code is described. Finally, we present two relevant cases which illustrate the performance of the model.

2. GOVERNING EQUATIONS

In this work, we consider fluid flow and heat transfer in a conjugate domain, Ω , which consists of pure fluid and porous regions, Ω_f and Ω_{por} , respectively. In Ω_f , the flow is governed by the continuity and Navier-Stokes equations, given by

$$\nabla \cdot \mathbf{u} = 0 \quad (1)$$

$$\rho_f \left[\frac{\partial \mathbf{u}}{\partial t} + \nabla \cdot (\mathbf{u}\mathbf{u}) \right] = -\nabla p + \mu_f \nabla^2 \mathbf{u} \quad (2)$$

The energy equation in the fluid region is given as

$$\rho_f c_{p,f} \left[\frac{\partial T}{\partial t} + \nabla \cdot (\mathbf{u}T) \right] = k_f \nabla^2 T \quad (3)$$

where the effects of viscous dissipation and heat generation are considered negligible since we are considering only laminar flows where the Eckert number is generally low and it is assumed that there are no internal heat sources.

While we do not consider pure solid regions in this work, we do require an energy equation for the solid constituent of the porous region for volume averaging. This is given as

$$\rho_s c_s \frac{\partial T}{\partial t} = k_s \nabla^2 T \quad (4)$$

In Ω_{por} the flow is governed by the volume-averaged counterparts of Eqs. (1)–(4). Let us define an averaging volume occupying the space V which contains fluid and solid, occupying the spaces V_f and V_s , respectively. Then, the volume-averaging operator is defined as

$$\langle \phi_k \rangle = \frac{1}{V} \int_{V_k} \phi_k dV \quad (5)$$

or

$$\langle \phi_k \rangle^k = \frac{1}{V_k} \int_{V_k} \phi_k dV \quad (6)$$

for extrinsic and intrinsic averages, respectively, where $k \in \{f, s\}$ denotes the phase in which the generic quantity ϕ_k is defined. Clearly, the two averages are related through the porosity $\varepsilon = V_f/V$.

Extrinsically averaging the continuity equation, Eq. (1), in accordance with the definitions above, we have [10, 20]

$$\nabla \cdot \langle \mathbf{u} \rangle = 0 \quad (7)$$

The extrinsically averaged momentum equation, arising from Eq. (2) with certain length-scale constraints [20] and the assumption of a constant porosity, is expressed as [10]

$$\rho_f \left[\frac{\partial \langle \mathbf{u} \rangle}{\partial t} + \frac{1}{\varepsilon} \nabla \cdot (\langle \mathbf{u} \rangle \langle \mathbf{u} \rangle) \right] = -\varepsilon \nabla \langle p \rangle^f + \mu_f \nabla^2 \langle \mathbf{u} \rangle - \frac{\varepsilon \mu_f}{K} \langle \mathbf{u} \rangle - \frac{\varepsilon \rho_f c_f}{\sqrt{K}} |\langle \mathbf{u} \rangle| \langle \mathbf{u} \rangle \quad (8)$$

where the final two terms on the right side of Eq. (8), known as the Darcy and Forchheimer terms, have been used empirically to close the set of equations as suggested by Vafai and Tien [10]. These terms describe the viscous and form drag interaction between the fluid and solid constituents in terms of volume-averaged quantities, rather than the pore-level quantities that arise directly from the averaging procedure.

The energy equations in Ω_{por} are derived under the assumption of local thermal nonequilibrium, leading to separate energy equations for the fluid and solid regions. These equations are given for the fluid and solid regions, respectively, as [21]

$$\rho_f c_{p,f} \left[\varepsilon \frac{\partial \langle T_f \rangle^f}{\partial t} + \nabla \cdot (\langle \mathbf{u} \rangle \langle T_f \rangle^f) \right] = k_{fe} \nabla^2 \langle T_f \rangle^f + h_{fs} a_{fs} (\langle T_s \rangle^s - \langle T_f \rangle^f) \quad (9)$$

$$(1 - \varepsilon) \rho_s c_s \frac{\partial \langle T_s \rangle^s}{\partial t} = k_{se} \nabla^2 \langle T_s \rangle^s - h_{fs} a_{fs} (\langle T_s \rangle^s - \langle T_f \rangle^f) \quad (10)$$

Here, the effective fluid and solid conductivities, k_{fe} and k_{se} , are used to close the set of equations and may include a component to account for the effects of thermal

dispersion. The final term in each of Eqs. (9) and (10) accounts for the convective heat exchange between the fluid and solid constituents within the porous medium.

3. INTERFACE CONDITIONS

The treatment of fluid-porous interfaces has been well studied over the years [14, 16–18, 22–25]. There is consensus in the literature that the most appropriate condition for the velocity at the interface, $\partial\Omega_{fl,por} = \Omega_{fl} \cap \Omega_{por}$, is to enforce its continuity, i.e.,

$$\mathbf{u}|_{fl} = \langle \mathbf{u} \rangle|_{por} \quad \text{on } \partial\Omega_{fl,por} \quad (11)$$

which was shown by Ochoa-Tapia and Whitaker [24]. Developing an appropriate condition for stress at the interface is more complicated, since it becomes difficult to construct a proper averaging volume containing only the fluid or only the porous region very near the interface. In this case, some terms involving the spatial porosity gradient, which are neglected in arriving at Eq. (8), may become important and lead to excess stresses at the interface. A stress-jump condition has been used successfully [17, 24], but, this approach requires parameters to be obtained from experimental data which may be unavailable for a particular flow configuration of interest. For interfaces parallel to the flow direction, Alazmi and Vafai [25] showed that taking the fluid stress to be continuous at the interface gave good results for the velocity profile and represented a reasonable compromise between the somewhat cumbersome stress-jump condition and the simplistic approximation of a constant velocity gradient on both sides of the interface. Thus, for the purposes of this work, we require that the stress carried by the fluid is continuous at the interface.

The stress tensors in the fluid and porous regions, in indicial notation, are given as

$$\sigma_{ij} = \mu_f \left(\frac{\partial u_i}{\partial x_j} + \frac{\partial u_j}{\partial x_i} \right) - p \delta_{ij} \quad (12)$$

$$\langle \sigma_{ij} \rangle = \mu_f \left(\frac{\partial \langle u_i \rangle}{\partial x_j} + \frac{\partial \langle u_j \rangle}{\partial x_i} \right) - \varepsilon \langle p \rangle^f \delta_{ij} \quad (13)$$

The stress on the pure fluid side of the interface, however, is carried partially by the fluid and partially by the solid constituent within the porous medium. Therefore, only a fraction ε of the stress on the pure fluid side is balanced by the fluid portion of the porous medium, resulting in the interface conditions [18, 23]

$$p|_{fl} = \langle p \rangle^f|_{por} \quad \text{on } \partial\Omega_{fl,por} \quad (14)$$

$$\mu_f \frac{\partial \mathbf{u}}{\partial \mathbf{n}} \Big|_{fl} = \frac{\mu_f}{\varepsilon} \frac{\partial \langle \mathbf{u} \rangle}{\partial \mathbf{n}} \Big|_{por} \quad \text{on } \partial\Omega_{fl,por} \quad (15)$$

where \mathbf{n} is the unit-normal vector at the fluid-porous interface.

In the energy equations, we take the temperature on the fluid side to be continuous with the average temperature on the porous side. Additionally, we require an energy balance over the surface to be satisfied. These conditions are stated mathematically as [18]

$$T|_{fl} = [\varepsilon \langle T_f \rangle^f + (1 - \varepsilon) \langle T_s \rangle^s]_{por} \quad \text{on} \quad \partial\Omega_{fl,por} \quad (16)$$

$$\left(k_f \frac{\partial T}{\partial \mathbf{n}} \right)_{fl} = \left(k_{fe} \frac{\partial \langle T_f \rangle^f}{\partial \mathbf{n}} + k_{se} \frac{\partial \langle T_s \rangle^s}{\partial \mathbf{n}} \right)_{por} \quad \text{on} \quad \partial\Omega_{fl,por} \quad (17)$$

4. DISCRETIZATION AND IMPLEMENTATION

4.1. Governing Equations

Discretization of the relevant governing equations is carried out for general, unstructured grids with arbitrary cell topology using a cell-centered finite-volume method. As such, we integrate the governing equations over an arbitrary control volume Ω_P having volume V_P which is bounded by the control surface $\partial\Omega_P$. It is assumed that $\partial\Omega_P$ may be expressed as the union of the discrete control surfaces $\partial\Omega_{ip}$, each of area A_{ip} , where $ip \in \{1, 2, \dots, N_{ip}\}$ and N_{ip} is the number of discrete control surfaces. For the governing equations in the fluid region, Eqs. (1)–(3), this results in

$$\sum_{ip=1}^{N_{ip}} \dot{m}_{ip} = 0 \quad (18)$$

$$\rho_f V_P \frac{\partial \mathbf{u}_P}{\partial t} + \sum_{ip=1}^{N_{ip}} \dot{m}_{ip} (\mathbf{u}_{ip} - \mathbf{u}_P) = - \sum_{ip=1}^{N_{ip}} p_{ip} \mathbf{n}_{ip} A_{ip} + \sum_{ip=1}^{N_{ip}} \mu_f \nabla \mathbf{u}|_{ip} \cdot \mathbf{n}_{ip} A_{ip} \quad (19)$$

$$\rho_f c_{p,f} V_P \frac{\partial T_P}{\partial t} + \sum_{ip=1}^{N_{ip}} \dot{m}_{ip} (T_{ip} - T_P) = \sum_{ip=1}^{N_{ip}} k_f \nabla T|_{ip} \cdot \mathbf{n}_{ip} A_{ip} \quad (20)$$

Note that Eq. (18) multiplied by \mathbf{u}_P and T_P has been subtracted from the discretized forms of Eqs. (2)–(3), respectively, to ensure a conservative method. Similarly, the discretized governing equations in the porous region arising from Eqs. (7)–(10) are given as

$$\sum_{ip=1}^{N_{ip}} \dot{m}_{ip} = 0 \quad (21)$$

$$\begin{aligned} \rho_f V_P \frac{\partial \langle \mathbf{u} \rangle_P}{\partial t} + \sum_{ip=1}^{N_{ip}} \frac{\dot{m}_{ip}}{\varepsilon} (\langle \mathbf{u} \rangle_{ip} - \langle \mathbf{u} \rangle_P) = & - \sum_{ip=1}^{N_{ip}} \varepsilon \langle p \rangle_{ip}^f \mathbf{n}_{ip} A_{ip} + \sum_{ip=1}^{N_{ip}} \mu_f \nabla \langle \mathbf{u} \rangle|_{ip} \cdot \mathbf{n}_{ip} A_{ip} \\ & - \frac{\varepsilon V_P \mu_f}{K} \langle \mathbf{u} \rangle_P - \frac{\varepsilon \rho_f V_P c_f}{\sqrt{K}} |\langle \mathbf{u} \rangle_P| \langle \mathbf{u} \rangle_P \end{aligned} \quad (22)$$

$$\varepsilon \rho_f c_{p,f} V_P \frac{\partial \langle T_f \rangle_P^f}{\partial t} + \sum_{ip=1}^{N_{ip}} c_{p,f} \dot{\mathbf{m}}_{ip} (\langle T_f \rangle_{ip}^f - \langle T_f \rangle_P^f) = \sum_{ip=1}^{N_{ip}} k_{fe} \nabla \langle T_f \rangle_{ip}^f \cdot \mathbf{n}_{ip} A_{ip} \quad (23)$$

$$+ h_{fs} a_{fs} V_P (\langle T_s \rangle_P^s - \langle T_f \rangle_P^f)$$

$$(1 - \varepsilon) \rho_s c_s V_P \frac{\partial \langle T_s \rangle_P^s}{\partial t} = \sum_{ip=1}^{N_{ip}} k_{se} \nabla \langle T_s \rangle_{ip}^s \cdot \mathbf{n}_{ip} A_{ip} - h_{fs} a_{fs} V_P (\langle T_s \rangle_P^s - \langle T_f \rangle_P^f) \quad (24)$$

Equations (18)–(24), presently in semidiscrete form, are second-order-accurate in space provided the points P and ip are taken to be at the centroids of the control volume and discrete control surfaces, respectively. Thus, to maintain a second-order method, all remaining interpolations used to cast the equations in fully discrete form must be accurate to a minimum of second-order. In general, interpolations will be in terms of both the cell-centered values of the dependent variables as well as their gradients. Terms involving the cell-centered values may be incorporated implicitly into the coefficient matrix describing the linearized problem, while other terms must be added explicitly to the right side of the linear system $\mathbf{Ax} = \mathbf{b}$. Generally, we aim to include as much implicit information as possible to enhance stability and convergence of the linearized problem to a solution of the nonlinear problem.

To obtain second-order accuracy in time, all partial derivatives with respect to time are computed using second-order backward differences, with the value at the present time step being implicit. The only exception to this is at the first time step, in which first-order backward differences must be used. For the spatial interpolations, the gradient vectors and Hessian tensors are reconstructed using the method proposed by Betchen and Straatman [26], which provides second-order-accurate gradients and first-order-accurate Hessian tensors. Convection terms are discretized using second-order upwind interpolations with the flux limiter of Venkatakrishnan [27], which was chosen because of its excellent convergence properties in comparison to many other limiters. The pressure terms in Eqs. (19) and (22) are evaluated using third-order-accurate spatial interpolations to obtain the pressure at the integration points. In general, a third-order interpolation using cell-centered values of a quantity ϕ and its derivatives is expressed as [26]

$$\begin{aligned} \phi_{ip} = & (1 - f_{ip})\phi_P + f_{ip}\phi_{nb} + \mathbf{D}_{f,ip} \cdot [(1 - f_{ip})\nabla\phi|_P + f_{ip}\nabla\phi|_{nb}] \\ & + \frac{1}{2} [\mathbf{D}_{f,ip}\mathbf{D}_{f,ip} - f_{ip}(1 - f_{ip})\mathbf{D}_{P,nb}\mathbf{D}_{P,nb}] \\ & : [(1 - f_{ip})\nabla\nabla\phi|_P + f_{ip}\nabla\nabla\phi|_{nb}] \end{aligned} \quad (25)$$

where the relevant displacement vectors are defined in Figure 1. Note that we have taken f_{ip} such that $\mathbf{D}_{P,nb} \cdot \mathbf{D}_{f,ip} = 0$, as suggested by Betchen and Straatman [26], in order to minimize the size of the correction associated with the interpolation from the point $\mathbf{x}_P + f_{ip}\mathbf{D}_{P,nb}$ to the point \mathbf{x}_{ip} .

Diffusion terms must be considered carefully, since in the form given in Eqs. (19)–(20) and Eqs. (22)–(24) there is no dependence on the cell-centered values and thus cannot be considered implicitly. One option is to decompose the diffusion

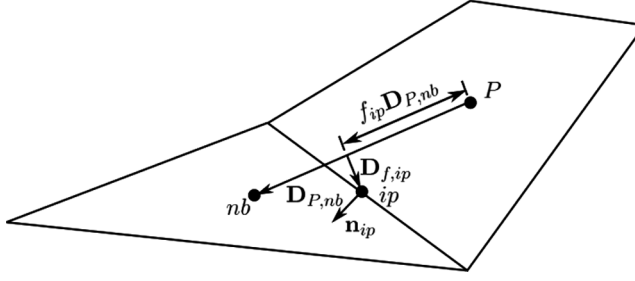


Figure 1. Illustration of two adjacent control volumes, P and nb , with the relevant geometric parameters noted.

term into normal and cross diffusion terms [28] or to use the approach of Demirdžić and Muzaferija [29], where a higher-order estimate of the gradient is used and the low-order estimate is subtracted explicitly. We employ a formulation similar to that of Demirdžić and Muzaferija [29] where the normal derivative at the integration point for a scalar ϕ is estimated as

$$\nabla\phi|_{ip} \cdot \mathbf{n}_{ip} = \overline{\nabla\phi}|_{ip} \cdot \mathbf{n}_{ip} + \left[\frac{\phi_{nb} - \phi_P}{\mathbf{D}_{P,nb} \cdot \mathbf{n}_{ip}} - \frac{((1-f_{ip})\nabla\phi|_P + f_{ip}\nabla\phi|_{nb}) \cdot \mathbf{D}_{P,nb}}{\mathbf{D}_{P,nb} \cdot \mathbf{n}_{ip}} \right] \quad (26)$$

where $\overline{\nabla\phi}|_{ip}$ denotes a second-order interpolation of $\nabla\phi$ to the integration point, given generally as

$$\overline{\nabla\phi}|_{ip} = (1-f_{ip})\nabla\phi|_P + f_{ip}\nabla\phi|_{nb} + \mathbf{D}_{f,ip} \cdot [(1-f_{ip})\nabla\nabla\phi|_P + f_{ip}\nabla\nabla\phi|_{nb}] \quad (27)$$

In Eq. (26), the first term in square brackets is a first-order estimate of the gradient at the integration point and may be treated implicitly, bringing stability to the solution method. Further, it may easily be shown using Taylor series that

$$\phi_{nb} - \phi_P = [(1-f_{ip})\nabla\phi|_P + f_{ip}\nabla\phi|_{nb}] \cdot \mathbf{D}_{P,nb} + O(\delta^3) \quad (28)$$

such that the term in square brackets in Eq. (26) is of the order δ^2 , as required to maintain the second-order accuracy of the given interpolation. Note that in this work, an inverse distance approximation of the gradient is employed in the last term of Eq. (26), rather than a simple mean as in [29], although both result in the same truncation error.

The mass flux through the discrete control surfaces, required to form the continuity equations and the convection terms, is computed as

$$\dot{m}_{ip} = \rho_f A_{ip} \langle \hat{\mathbf{u}} \rangle_{ip} \cdot \mathbf{n}_{ip} \quad (29)$$

noting that $\langle \mathbf{u} \rangle_{ip} = \mathbf{u}_{ip}$ in the fluid region. The advecting velocity, $\langle \hat{\mathbf{u}} \rangle_{ip}$, is computed using the approach of Rhie and Chow [30], which uses a specially constructed momentum equation to ensure coupling between the velocity and pressure fields. As an illustration, let us consider the x -momentum equation, given for the control

volume P :

$$a_P \langle u \rangle_P = \sum_{ip=1}^{N_{ip}} a_{nb,ip} \langle u \rangle_{nb,ip} + b_P - \varepsilon V_P \frac{\partial \langle p \rangle^f}{\partial x} \Big|_P = \langle \tilde{\mathbf{u}} \rangle_P - \varepsilon V_P \frac{\partial \langle p \rangle^f}{\partial x} \Big|_P \quad (30)$$

where $\varepsilon = 1$ in the fluid region. Similarly, for the volume nb sharing an integration point ip with the volume P , we may write

$$a_{nb} \langle u \rangle_{nb} = \langle \tilde{\mathbf{u}} \rangle_{nb} - \varepsilon V_{nb} \frac{\partial \langle p \rangle^f}{\partial x} \Big|_{nb} \quad (31)$$

By analogy, we may write a similar equation for a “virtual” control volume centered about the integration point ip , to obtain an estimate of the advecting velocity $\langle \hat{\mathbf{u}} \rangle_{ip}$, given as

$$\langle \hat{\mathbf{u}} \rangle_{ip} = \frac{\langle \tilde{\mathbf{u}} \rangle_{ip}}{a_{ip}} - \frac{\varepsilon V_{ip}}{a_{ip}} \frac{\partial \langle p \rangle^f}{\partial x} \Big|_{ip} \quad (32)$$

where $V_{ip} = (V_P + V_{nb})/2$ and $a_{ip} = (a_P + a_{nb})/2$. The value of $\langle \tilde{\mathbf{u}} \rangle_{ip}$ is then found by interpolation using the values of $\langle \tilde{\mathbf{u}} \rangle_P$ and $\langle \tilde{\mathbf{u}} \rangle_{nb}$ at the surrounding control volumes. When P and nb are both located in the same region (i.e., they are both porous or both fluid), we may assume that $a_P \approx a_{nb} \approx a_{ip}$ and $V_P \approx V_{nb} \approx V_{ip}$ in Eqs. (30)–(31) and then interpolate $\langle \tilde{\mathbf{u}} \rangle$ to the integration point from the values at the neighboring control volumes. This results in

$$\langle \hat{\mathbf{u}} \rangle_{ip} = \overline{\langle \mathbf{u} \rangle}_{ip} - \frac{\varepsilon V_{ip}}{a_{ip}} \left(\frac{\partial \langle p \rangle^f}{\partial x} \Big|_{ip} - \overline{\frac{\partial \langle p \rangle^f}{\partial x}} \Big|_{ip} \right) \quad (33)$$

where the overbar again indicates a second-order interpolation to the integration point. Forming similar equations for the advecting velocity in the remaining directions, we may compute the mass flux as

$$\dot{m}_{ip} = \rho_f A_{ip} [\overline{\langle \mathbf{u} \rangle}_{ip} \cdot \mathbf{n}_{ip} - \varepsilon \hat{d}_{ip} (\nabla \langle p \rangle^f|_{ip} - \overline{\nabla \langle p \rangle^f}|_{ip}) \cdot \mathbf{n}_{ip}] \quad (34)$$

where \hat{d}_{ip} is the average of V_{ip}/a_{ip} in each of the coordinate directions, weighted by the magnitude of the normal vector in that direction. Then, using Eq. (26) for $\nabla \langle p \rangle^f|_{ip} \cdot \mathbf{n}_{ip}$ the second-order interpolation of the pressure gradient to the interface cancels out, leaving

$$\begin{aligned} \dot{m}_{ip} = \rho_f A_{ip} \Bigg(\overline{\langle \mathbf{u} \rangle}_{ip} \cdot \mathbf{n}_{ip} - \varepsilon \hat{d}_{ip} \Bigg\{ \frac{\langle p \rangle_{nb}^f - \langle p \rangle_P^f}{\mathbf{D}_{P,nb} \cdot \mathbf{n}_{ip}} \\ - \frac{[(1 - f_{ip}) \nabla \langle p \rangle^f|_P + f_{ip} \nabla \langle p \rangle^f|_{nb}] \cdot \mathbf{D}_{P,nb}}{\mathbf{D}_{P,nb} \cdot \mathbf{n}_{ip}} \Bigg\} \Bigg) \end{aligned} \quad (35)$$

Thus, we have now managed to incorporate the pressure into the calculation of the mass flux at the integration point, which allows us to express the continuity equation in terms of both velocity and pressure. During the solution procedure, the pressure term in Eq. (35) acts to smooth out spurious oscillations in the pressure field, while in a converged solution, this term will vanish to within the second-order truncation error of the numerical scheme. It should also be noted that we solve the mass and momentum equations simultaneously as a coupled set rather than solve in a segregated manner as in [28, 31].

4.2. Interface Conditions

At the interface between a fluid and porous region, care must be taken in obtaining estimates of the pressure, advecting velocity, as well as the diffusive and advective fluxes, to ensure that they are physically reasonable and do not induce spurious oscillations in any of the solution fields. When estimating the advecting velocity in either the pure fluid or porous region, we are able to assume that the active coefficients, a_P and a_{nb} , on either side of a control surface are approximately equal, simplifying the expression for $\langle \hat{\mathbf{u}} \rangle_{ip}$ substantially. In the case where one of the volumes is fluid and the other is porous, this simplification is invalid as a result of the potentially large Darcy and Forchheimer terms present on the porous side of the interface. Additionally, the advective momentum flux on the fluid side of an interface takes on the form $\dot{m}_{ip} \langle \mathbf{u} \rangle_{ip} / \varepsilon$, while in the remainder of the fluid region it is of the form $\dot{m}_{ip} \langle \mathbf{u} \rangle_{ip}$. As a result, special consideration must be made for the pressure at the interface to account for its rapid change as the fluid approaches the interface, such that the pressure forces balance the differing advective fluxes at the interface in comparison to that a small distance away from the interface. Also, the values of velocity and temperature at the interface must be calculated such that they correctly satisfy the proper diffusion balance equation.

Since we are developing special methods for estimating the velocity, temperature, and pressure at the interface, it is important to ensure that these values are taken into account when reconstructing the gradient vectors and Hessian tensors. As a result, any fluid-porous interfaces are effectively treated as boundaries in the gradient and Hessian reconstruction, in which the value of the independent variable is specified and the gradient is extrapolated in the same manner as described by Betchen and Straatman [26] for standard boundaries. However, as will be described later, the interface value used in the gradient and Hessian reconstruction is not always the same as that used for other purposes, such as advective fluxes or pressure forces.

4.2.1. Diffusive and advective terms. Let us first consider a general diffusion balance at an interface between two regions, given as

$$\Gamma_P \nabla \phi|_{ip,P} \cdot \mathbf{n}_{ip} = \Gamma_{nb} \nabla \phi|_{ip,nb} \cdot \mathbf{n}_{ip} \quad (36)$$

where Γ_i is the diffusion coefficient for the volume i and the subscript ip, i denotes a quantity evaluated at the integration point, from the side of volume i . The normal derivative at the integration point can be formed by extrapolating the cell-centered value at point P to a point which is located on a line through the integration point,

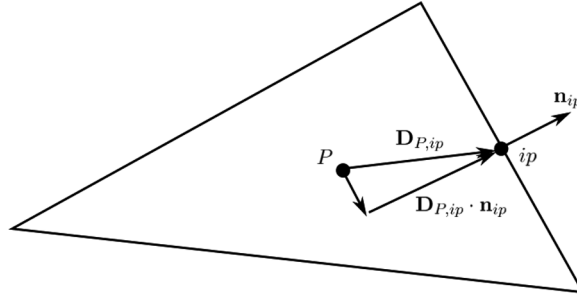


Figure 2. Illustration of a control volume, P , with the relevant geometric parameters for evaluating the normal derivative noted.

in the direction of the normal to the face as illustrated in Figure 2. Using a finite difference approximation along this line for the volume P , it is determined that a second-order approximation of the normal derivative at the integration point is given as

$$\nabla \phi|_{ip,P} \cdot \mathbf{n}_{ip} = \frac{\phi_{ip} - [\phi_P + \nabla \phi|_P \cdot (\mathbf{D}_{P,ip} - (\mathbf{D}_{P,ip} \cdot \mathbf{n}_{ip})\mathbf{n}_{ip})]}{\mathbf{D}_{P,ip} \cdot \mathbf{n}_{ip}} \quad (37)$$

where $\mathbf{D}_{P,ip} = \mathbf{x}_{ip} - \mathbf{x}_P$. Then, considering two volumes, P and nb , on opposite sides of an interface, we may formulate an expression for the value of ϕ at the integration point which satisfies the diffusion balance by substituting the expression given in Eq. (37) and an analogous expression for the volume nb into the general diffusion balance given in Eq. (36). As a result, it is shown that

$$\begin{aligned} \phi_{ip} = & \frac{\Gamma_{nb}(\mathbf{D}_{P,ip} \cdot \mathbf{n}_{ip})}{\Gamma_{nb}(\mathbf{D}_{P,ip} \cdot \mathbf{n}_{ip}) - \Gamma_P(\mathbf{D}_{nb,ip} \cdot \mathbf{n}_{ip})} \phi_{nb} \\ & - \frac{\Gamma_P(\mathbf{D}_{nb,ip} \cdot \mathbf{n}_{ip})}{\Gamma_{nb}(\mathbf{D}_{P,ip} \cdot \mathbf{n}_{ip}) - \Gamma_P(\mathbf{D}_{nb,ip} \cdot \mathbf{n}_{ip})} \phi_P \\ & + \frac{\Gamma_{nb}(\mathbf{D}_{P,ip} \cdot \mathbf{n}_{ip})(\mathbf{D}_{nb,ip} - (\mathbf{D}_{nb,ip} \cdot \mathbf{n}_{ip})\mathbf{n}_{ip})}{\Gamma_{nb}(\mathbf{D}_{P,ip} \cdot \mathbf{n}_{ip}) - \Gamma_P(\mathbf{D}_{nb,ip} \cdot \mathbf{n}_{ip})} \cdot \nabla \phi|_{nb} \\ & - \frac{\Gamma_P(\mathbf{D}_{nb,ip} \cdot \mathbf{n}_{ip})(\mathbf{D}_{P,ip} - (\mathbf{D}_{P,ip} \cdot \mathbf{n}_{ip})\mathbf{n}_{ip})}{\Gamma_{nb}(\mathbf{D}_{P,ip} \cdot \mathbf{n}_{ip}) - \Gamma_P(\mathbf{D}_{nb,ip} \cdot \mathbf{n}_{ip})} \cdot \nabla \phi|_P \end{aligned} \quad (38)$$

where $\mathbf{D}_{nb,ip} = \mathbf{x}_{ip} - \mathbf{x}_{nb}$. Equation (38) may then be substituted back into Eq. (37) to obtain the normal derivative, which is used in forming the diffusion terms. The result is summarized as

$$\begin{aligned} \nabla \phi|_{ip,P} \cdot \mathbf{n}_{ip} = & \frac{\phi_{nb} - \phi_P}{(\mathbf{D}_{P,ip} \cdot \mathbf{n}_{ip}) - \Gamma_P/\Gamma_{nb}(\mathbf{D}_{nb,ip} \cdot \mathbf{n}_{ip})} \\ & + \frac{(\mathbf{D}_{nb,ip} - (\mathbf{D}_{nb,ip} \cdot \mathbf{n}_{ip})\mathbf{n}_{ip})}{(\mathbf{D}_{P,ip} \cdot \mathbf{n}_{ip}) - \Gamma_P/\Gamma_{nb}(\mathbf{D}_{nb,ip} \cdot \mathbf{n}_{ip})} \cdot \nabla \phi|_{nb} \\ & - \frac{(\mathbf{D}_{P,ip} - (\mathbf{D}_{P,ip} \cdot \mathbf{n}_{ip})\mathbf{n}_{ip})}{(\mathbf{D}_{P,ip} \cdot \mathbf{n}_{ip}) - \Gamma_P/\Gamma_{nb}(\mathbf{D}_{nb,ip} \cdot \mathbf{n}_{ip})} \cdot \nabla \phi|_P \end{aligned} \quad (39)$$

Note that the first two terms in Eq. (38) and the first term in Eq. (39) are equivalent to those given by Betchen et al. [18], while the remaining terms ensure second-order accuracy when the grid is nonorthogonal. In cases where the grid is orthogonal $\mathbf{D}_{P,ip} - (\mathbf{D}_{P,ip} \cdot \mathbf{n}_{ip})\mathbf{n}_{ip} = \mathbf{D}_{nb,ip} - (\mathbf{D}_{nb,ip} \cdot \mathbf{n}_{ip})\mathbf{n}_{ip} = 0$, so these additional terms will be identically zero. When using Eq. (39) in diffusive terms, the first term is treated implicitly, while the remaining terms must be treated explicitly.

For the particular case of the stress balance at the interface, we may take $\Gamma_P = \mu_f$ and $\Gamma_{nb} = \mu_f/\varepsilon$ when volume P is on the fluid side, or the reverse when volume P is on the porous side of the interface. Substituting these values into Eq. (39), yields the appropriate value of the normal derivative at the interface, which is used to compute the diffusion terms in the momentum equation. Additionally, the value of the velocity at the integration point is computed using Eq. (38), which is used to provide a physically realistic estimate of the advective momentum transfer through the control surface located at an interface.

In the energy equations, we implement the parallel conduction model proposed by Betchen et al. [18], given for an arbitrarily oriented interface as

$$q_f'' = \varepsilon k_f \nabla T|_{fl} \cdot \mathbf{n}_{ip} = \varepsilon k_{fe} \nabla \langle T_f \rangle' |_{por} \cdot \mathbf{n}_{ip} \quad \text{on} \quad \partial\Omega_{fl,por} \quad (40)$$

$$q_s'' = (1 - \varepsilon) k_f \nabla T|_{fl} \cdot \mathbf{n}_{ip} = \varepsilon k_{se} \nabla \langle T_s \rangle^s |_{por} \cdot \mathbf{n}_{ip} \quad \text{on} \quad \partial\Omega_{fl,por} \quad (41)$$

for the conduction heat flux within the fluid and solid constituents, respectively. Note that the addition of Eqs. (40)–(41) satisfy the interfacial heat flux balance given by Eq. (17) and may be implemented quite simply using Eqs. (38)–(39) to obtain the advected temperature at an interface. These equations are also used in forming diffusive fluxes at interfaces; however, it must be noted that on the fluid side of the interface, the heat flux through the interface is the sum of q_f'' and q_s'' given in Eqs. (40)–(41). Additionally, when computing the fluid temperature gradients and Hessians, the interface temperature on the fluid side of the interface is defined by the average given in Eq. (16), while on the porous side it is defined in the same way as the advected temperature.

4.2.2. Interface pressure. In order to compute the pressure forces in the momentum equations as well as the mass flux at the integration points for volumes adjacent to interfaces, the interface pressure must be considered carefully. The first issue that arises is the generally discontinuous nature of the pressure gradient across the interface as a result of the presence of the Darcy and Forchheimer terms on the porous side, which results in a greater pressure gradient required to drive the flow. Additionally, as a result of reduction in flow area as the fluid flows from the fluid region into the porous region, the advecting velocity undergoes a rapid change, which must be balanced by appropriate pressure forces. Let us consider an example, illustrated in Figure 3, in which fluid is flowing into a porous region from a pure fluid region. Following a momentum balance on the narrow control volume on the fluid side of the interface, neglecting any mass flux from the sides of width δ^- , the pressure at ip is found to be [18]

$$p_{ip} = p_{ip^-} - \frac{1 - \varepsilon \dot{m}_{ip} \langle \mathbf{u} \rangle_{ip} \cdot \mathbf{n}_{ip}}{\varepsilon A_{ip}} \quad (42)$$

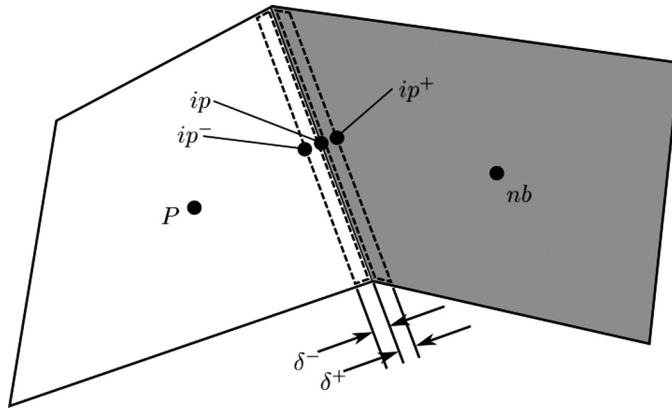


Figure 3. Illustration of two control volumes on opposite sides of an fluid-porous interface, P being fluid and nb being porous (indicated by shading), with the relevant partial control volumes indicated with dashed lines.

while a similar momentum balance on the porous side of the interface indicates that

$$p_{ip} = p_{ip^+} \quad (43)$$

where p_{ip^-} and p_{ip^+} are computed using third-order Taylor series extrapolations from P and nb , respectively. Then, letting $\delta^-, \delta^+ \rightarrow 0$ gives us an estimate of the interface pressure at an infinitesimally small distance from ip on either side of the interface that accounts for the change in advecting velocity at the interface. Clearly, this means that a different pressure will be used in the fluid and porous regions to compute the pressure forces in the momentum equations. Thus, while we do not directly enforce the pressure continuity condition listed in Eq. (14), it is implied that it is satisfied at ip ; however, we evaluate the pressure forces using pressures very small distances away from ip to avoid any difficulties associated with the discontinuous gradient at this point. As will be shown, it has been found that this approach is necessary on nonorthogonal grids to avoid spurious oscillations in the velocity field.

When computing the gradients at the cell centroids, however, it does not make physical sense to take the pressure at the integration point to be the interface pressure computed above, since this would artificially change the magnitude of the gradient in the fluid region. While Betchen et al. [18] were able to use the corrected pressure in computing gradients, this is due to the structured, orthogonal framework of that code, which blends this estimate with an estimate of the gradient from the other side of the control volume. In the present nonorthogonal code, the gradient and Hessian tensors in each region are tightly coupled together, meaning that an over or underestimate of the gradient adjacent to the interface will propagate itself throughout that domain. Therefore, when computing the gradients and Hessians at volumes adjacent to an interface, we take the pressures on either side to be the pressures extrapolated using third-order Taylor series to the points ip^- and ip^+ with $\delta^-, \delta^+ \rightarrow 0$. From a physical perspective, this gives a better estimate of the gradient

and Hessian over the control volume as a whole, since the rapid change in pressure described by Eq. (42) occurs over such a small portion of that volume. Again, we will show that this method is required to obtain a realistic estimate of the pressure gradient in volumes adjacent to interfaces and to avoid spurious oscillations in the velocity field.

4.2.3. Advecting velocity. At fluid-porous interfaces, special consideration must also be given to the advecting velocity, since the assumption $a_P \approx a_{nb} \approx a_{ip}$ is not valid due to the potentially large Darcy and Forchheimer terms on the porous side of the interface. In this case, the interpolation of $\langle \tilde{\mathbf{u}} \rangle$ to the integration point based on Eqs. (30) and (31) takes on the form

$$\begin{aligned} \langle \tilde{\mathbf{u}} \rangle_{ip} = & (1 - f_{ip})a_P \langle \mathbf{u} \rangle_P + f_{ip}a_{nb} \langle \mathbf{u} \rangle_{nb} \\ & + \mathbf{D}_{f,ip} \cdot [(1 - f_{ip})a_P \nabla \langle \mathbf{u} \rangle|_P + f_{ip}a_{nb} \nabla \langle \mathbf{u} \rangle|_{nb}] + \overline{\left(\varepsilon V \frac{\partial \langle p \rangle^f}{\partial x} \right)} \Big|_{ip} \end{aligned} \quad (44)$$

where again the overbar indicates a second-order interpolation to the integration point. Using this expression in Eq. (32) results in

$$\begin{aligned} \langle \hat{\mathbf{u}} \rangle_{ip} = & (1 - f_{ip}) \frac{a_P}{a_{ip}} \langle \mathbf{u} \rangle_P + f_{ip} \frac{a_{nb}}{a_{ip}} \langle \mathbf{u} \rangle_{nb} \\ & + \mathbf{D}_{f,ip} \cdot \left[(1 - f_{ip}) \frac{a_P}{a_{ip}} \nabla \langle \mathbf{u} \rangle|_P + f_{ip} \frac{a_{nb}}{a_{ip}} \nabla \langle \mathbf{u} \rangle|_{nb} \right] \\ & - \frac{V_{ip}}{a_{ip}} \left[\varepsilon_{ip} \frac{\partial \langle p \rangle^f}{\partial x} \Big|_{ip} - \frac{1}{V_{ip}} \overline{\left(\varepsilon V \frac{\partial \langle p \rangle^f}{\partial x} \right)} \Big|_{ip} \right] \end{aligned} \quad (45)$$

Since $\partial \langle p \rangle^f / \partial x$ is generally expected to be discontinuous across fluid-porous interfaces, we make the following assumption regarding the pressure gradient at the integration point:

$$\varepsilon_{ip} \frac{\partial \langle p \rangle^f}{\partial x} \Big|_{ip} = \frac{1}{2V_{ip}} \left(\varepsilon_P V_P \frac{\partial \langle p \rangle^f}{\partial x} \Big|_{ip^-} + \varepsilon_{nb} V_{nb} \frac{\partial \langle p \rangle^f}{\partial x} \Big|_{ip^+} \right) \quad (46)$$

which is a volume-weighted average of the porosity multiplied by the pressure gradient, estimated from either side of the integration point. Additionally, the interpolated pressure gradient term in Eq. (45) is treated simply as the mean of the values on either side of the integration point, i.e.,

$$\overline{\left(\varepsilon V \frac{\partial \langle p \rangle^f}{\partial x} \right)} \Big|_{ip} = \frac{1}{2} \left(\varepsilon_P V_P \frac{\partial \langle p \rangle^f}{\partial x} \Big|_{ip^-} + \varepsilon_{nb} V_{nb} \frac{\partial \langle p \rangle^f}{\partial x} \Big|_{ip^+} \right) \quad (47)$$

Combining Eqs. (46) and (47) with Eq. (45) and forming similar equations in the remaining coordinate directions, we arrive at an estimate of the mass flux at the

integration point, given as

$$\begin{aligned} \dot{m}_{ip} = \rho_f A_{ip} \left\{ \overline{\langle \mathbf{u} \rangle'}_{ip} \cdot \mathbf{n}_{ip} - \hat{a}_{ip} \left[\frac{1}{2} \frac{\varepsilon_P V_P}{V_{ip}} (\nabla \langle p \rangle^f|_{ip^-} - \overline{\nabla \langle p \rangle^f}|_{ip^-}) \cdot \mathbf{n}_{ip} \right. \right. \\ \left. \left. + \frac{1}{2} \frac{\varepsilon_{nb} V_{nb}}{V_{ip}} (\nabla \langle p \rangle^f|_{ip^+} - \overline{\nabla \langle p \rangle^f}|_{ip^+}) \cdot \mathbf{n}_{ip} \right] \right\} \end{aligned} \quad (48)$$

where $\overline{\langle \mathbf{u} \rangle}'_{ip}$ is a special interpolation to the integration point which is weighted by the active coefficients and is defined as

$$\begin{aligned} \overline{\langle \mathbf{u} \rangle}'_{ip} = (1 - f_{ip}) \frac{a_P}{a_{ip}} \langle \mathbf{u} \rangle_P + f_{ip} \frac{a_{nb}}{a_{ip}} \langle \mathbf{u} \rangle_{nb} \\ + \mathbf{D}_{f,ip} \cdot \left[(1 - f_{ip}) \frac{a_P}{a_{ip}} \nabla \langle \mathbf{u} \rangle|_P + f_{ip} \frac{a_{nb}}{a_{ip}} \nabla \langle \mathbf{u} \rangle|_{nb} \right] \end{aligned} \quad (49)$$

As before, the pressure gradients in the direction of the unit normal at the integration point are estimated using Eq. (26), resulting in

$$\begin{aligned} \dot{m}_{ip} = \rho_f A_{ip} \left\{ \overline{\langle \mathbf{u} \rangle}'_{ip} \cdot \mathbf{n}_{ip} - \hat{a}_{ip} \left[\frac{1}{2} \frac{\varepsilon_P V_P}{V_{ip}} \left(\frac{\langle p \rangle^f_{ip} - \langle p \rangle^f_P}{\mathbf{D}_{P,ip} \cdot \mathbf{n}_{ip}} - \frac{\nabla \langle p \rangle^f|_P \cdot \mathbf{D}_{P,ip}}{\mathbf{D}_{P,ip} \cdot \mathbf{n}_{ip}} \right) \right. \right. \\ \left. \left. + \frac{1}{2} \frac{\varepsilon_{nb} V_{nb}}{V_{ip}} \left(\frac{\langle p \rangle^f_{ip} - \langle p \rangle^f_{nb}}{\mathbf{D}_{nb,ip} \cdot \mathbf{n}_{ip}} - \frac{\nabla \langle p \rangle^f|_{nb} \cdot \mathbf{D}_{nb,ip}}{\mathbf{D}_{nb,ip} \cdot \mathbf{n}_{ip}} \right) \right] \right\} \end{aligned} \quad (50)$$

5. RESULTS AND DISCUSSION

In this section, we consider two particular configurations involving coupled fluid and porous regions and solve the flows using the numerical model described previously. The first problem to be solved is that of plane flow through a parallel-plate channel with a porous plug inserted some distance from the inlet. At high Reynolds numbers [$\text{Re}_H \geq O(100)$], this problem is typically quite challenging to solve numerically, and special consideration of the interface conditions is necessary [18]. In this case we solve for $\text{Re}_H = 1,000$ and find that accurate results are obtained at all locations, including the interface. This problem is used to demonstrate the effectiveness of the present formulation on nonorthogonal grids as well as to show the problems that occur when modified formulations are employed, even on orthogonal grids. The second problem involves a porous heat sink, which demonstrates the effectiveness of the conjugate heat transfer model in geometries that cannot be discretized using orthogonal grids.

5.1. Porous Plug Flow

The porous plug problem considered here is identical to that considered by Betchen et al. [18] and is illustrated schematically in Figure 4. In this case we are interested in computing the flow field for $\text{Re}_H = 1,000$ and $\text{Da} = 10^{-2}$, since the

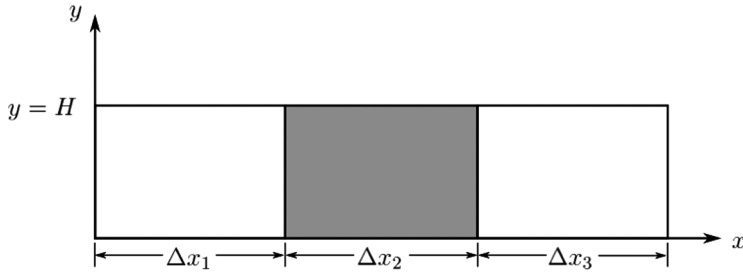


Figure 4. Schematic diagram of the porous plug case, where the shaded region indicates the porous subdomain.

pressure correction term given in Eq. (42) will be rather large and thus challenging to solve numerically. This particular case is discretized using both hexahedral and triangular prismatic volumes, shown in Figure 5, in order to demonstrate the effectiveness of the nonorthogonal correction terms introduced in this article, since these terms will be relatively large in the case of the triangular prismatic grids and identically zero in the case of the hexahedral grids.

The cases using hexahedral grids are configured in the same way as in [18], where the lengths shown in Figure 4 were specified as $\Delta x_1 = \Delta x_2 = 5H$ and

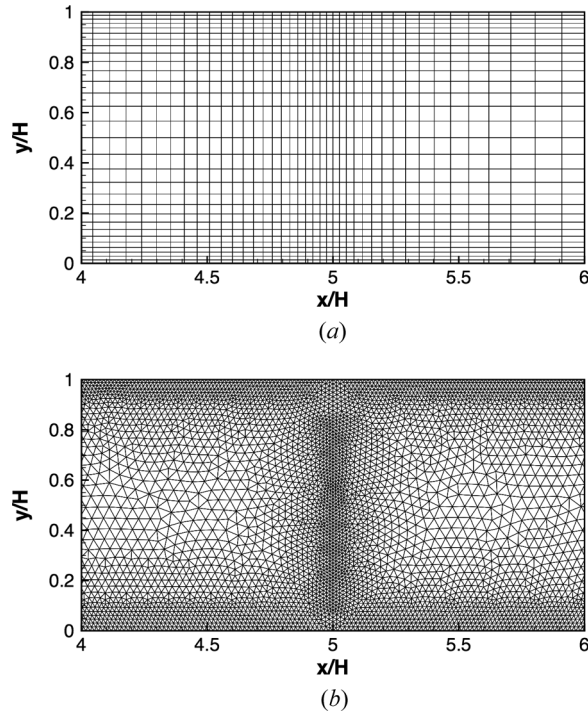


Figure 5. Plots of (a) hexahedral and (b) triangular prismatic grids, near an interface, used for the porous plug case.

$\Delta x_3 = 50H$. In this case the large value of Δx_3 is chosen to ensure fully developed conditions at the outlet. Although this case is two-dimensional, it is discretized using three-dimensional grids with a single row of volumes in the z direction with symmetry conditions imposed on the planes of constant z . The velocity boundary conditions consist of a fully developed plane channel flow specified at the inlet boundary, $x=0$, fully developed conditions at the outlet boundary, $x=60H$, and zero velocity at the channel walls, $y=0$ and $y=H$. The pressure was specified as zero at the outlet boundary to set the pressure level, while pressure was extrapolated to all other boundaries.

Using hexahedral grids, it is possible to create volumes near the outlet boundary which are very long in the flow direction in order to greatly reduce the number of volumes in the portion of the domain downstream of the porous plug. Although these volumes have a very high aspect ratio, accuracy is maintained since the flow is nearly fully developed. With triangular prismatic grids this approach is not practical, thus a great number of volumes are required to compute the downstream flow, which is not generally of interest. To avoid this issue we instead choose $\Delta x_3 = 5H$ and implement a velocity boundary condition based on an application of the continuity equation at the outlet face. In this case, since the primary flow is in the x direction, the velocity components in the y and z directions are simply extrapolated to the outlet, while the pressure is set to zero. Based on the continuity equation we may state that

$$\left. \frac{\partial u}{\partial x} \right|_{ip} = - \left(\frac{\partial v}{\partial y} + \frac{\partial w}{\partial z} \right)_{ip} \quad (51)$$

Then, since $\mathbf{n}_{ip} = \mathbf{i}$, Eq. (37) may be applied to find $\partial u / \partial x$ at the integration point, which results in an expression for the integration point velocity given as

$$u_{ip} = u_P + \nabla u|_P \cdot (\mathbf{D}_{P,ip} - (\mathbf{D}_{P,ip} \cdot \mathbf{i})\mathbf{i}) - \left(\frac{\partial v}{\partial y} + \frac{\partial w}{\partial z} \right)_{ip} (\mathbf{D}_{P,ip} \cdot \mathbf{i}) \quad (52)$$

which is used to specify the velocity component in the x direction at the outlet boundary.

Grid independence studies were performed for each volume type, where the total number of volumes was repeatedly doubled until all quantities of interest changed by less than a specified amount. In this case, we wish to obtain results which are grid-independent to within 1%. The results of the present grid-independence studies are summarized in Tables 1 and 2. In general, it was found that obtaining an overall

Table 1. Grid independence study for the porous plug case discretized using hexahedral grids

$N_x \times N_y$	Δp	% difference	$u(2.5H, 0.5H)/U$	% difference
35×21	1,463.41	N/A	1.476	N/A
50×30	1,466.36	0.2	1.494	1.2
70×42	1,469.27	0.2	1.497	0.2

Note that the number of control volumes is given for the porous plug section only and that the pressure difference is given across the full length of the domain.

Table 2. Grid independence study for the porous plug case discretized using triangular prismatic grids

δ_w	N_{por}	Δp	% difference	$u(2.5H, 0.5H)/U$	% difference
0.0375	4,644	1,382.83	N/A	1.486	N/A
0.0227	9,272	1,394.43	0.8	1.490	0.3
0.0129	1,8726	1,400.07	0.4	1.494	0.3

Note that the number of control volumes is given for the porous plug section only and that the pressure difference is given across the full length of the domain (which is truncated in comparison to the hexahedral grid case). Also note that for all grids, the growth rate was 10% per row with a maximum characteristic grid size of $4\delta_w$.

pressure drop across the domain that was grid-independent did not always yield velocity fields which were also grid-independent. Thus, in addition to the pressure drop across the domain, we also consider the velocity at the point $(2.5H, 0.5H)$, which is associated with how well momentum diffusion is resolved in the upstream channel and should approach 1.5 as the solution is well resolved. Using hexahedral grids it was found that using 35×21 control volumes in the porous region, with similar grid densities in the fluid regions, was sufficient to obtain grid-independent results for the pressure drop, but that further refinement was required to obtain grid-independent velocity results. A grid with 50×30 volumes in the porous region was found to be sufficiently refined for the velocity field to be grid-independent, therefore this grid is used for all subsequent calculations. Note that in all of these cases, the volumes adjacent to the interface and walls were refined in comparison to those in the interior of the domain, as shown in Figure 5a.

Using the prismatic grids, shown in Figure 5b, it was found that about 4,644 volumes were needed to discretize the porous region in order to achieve results for pressure and velocity fields that were grid-independent, in comparison to the 1,500 volumes for the hexahedral grids. This is reasonable, however, due to the nonorthogonal nature of these grids as well as the smaller area occupied by a triangle in comparison to a square of the same characteristic dimension. While the prismatic grid containing 4,644 volumes was sufficient to obtain grid-independent results, it proved challenging in some locations to interpolate a smooth curve along the channel centerline. As a result, the grid containing 9,272 volumes in the porous region has been used for subsequent calculations, since the volumes near the centerline are smaller and lead to more accurate interpolations for plotting purposes.

Figure 6 shows the results computed using the two different grid types described above for the streamwise velocity component along the line $y/H=0.5$ on the interval $x/H \in [2.5, 12.5]$ in addition to the results obtained by Betchen et al. [18]. It is clear from this figure that the results obtained using the two different grid types are in quite good agreement with one another, indicating that the terms which account for the nonorthogonality of the grid are accurate. Additionally, comparing to the results given by Betchen et al. [18] for the same case, we see similar results, although the profiles near the interfaces are slightly different due to the different treatment of the pressure at the interface. While Betchen et al. [18] blend the pressure obtained using Eqs. (42) and (43) to arrive at an estimate for the interface pressure and use this pressure to find the pressure gradient, we use different interface pressures on either side of the interface and do not use the corrected

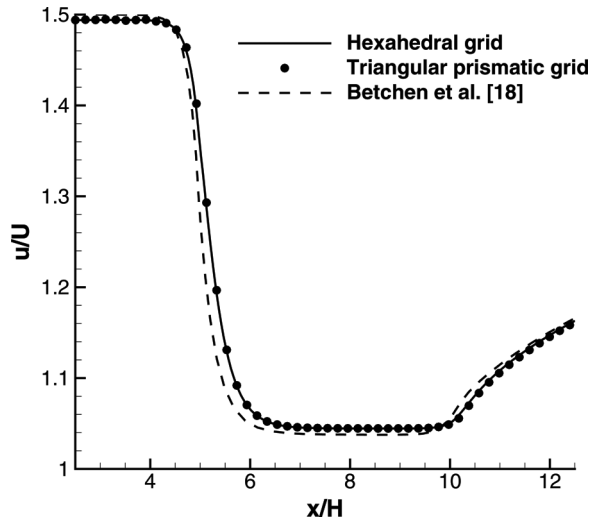


Figure 6. Plot of the streamwise velocity component for the porous plug problem with $Re_H = 1,000$ and $Da = 10^{-2}$ as a function of position along the line $y/H = 0.5$ on the interval $x/H \in [2.5, 12.5]$ using the two grid types in comparison to results from Betchen et al. [18].

pressure to reconstruct the pressure gradient field. Thus, the pressure forces on the fluid at the interface are slightly different, leading to a slight difference in the velocity field.

In addition to evaluating the effects of grid type, we also wish to evaluate the impact of the present form of the pressure correction in comparison to other possible treatments of the interface pressure. To do so, we introduce the following modified schemes.

1. Use a standard second-order interpolation for p_{ip} at interfaces and perform no special pressure correction in the momentum equations.
2. Take the interface pressure to be the average of the estimates given in Eqs. (42) and (43) (as in [18]) and use this pressure for both the gradient reconstruction and the pressure forces in the momentum equations.

Results shown in Figures 7a and 7b indicate that the use of either of these modified schemes yields highly unrealistic results in the vicinity of the interface, and it is clear that the velocity has become quite decoupled from the pressure field. The failure of the first modified method indicates that a pressure correction is indeed required, while failure of the second modified method shows that the corrected pressure should not be used for reconstructing the gradients for reasons described previously. In summary, this indicates that the interface pressure conditions proposed in this work are indeed required to obtain reasonable results for high Re_H on unstructured grids, even if orthogonal, due to issues associated with the gradient reconstruction.

It should also be noted that the convergence of the proposed method is not significantly slower than that of the first modified method and that it is significantly

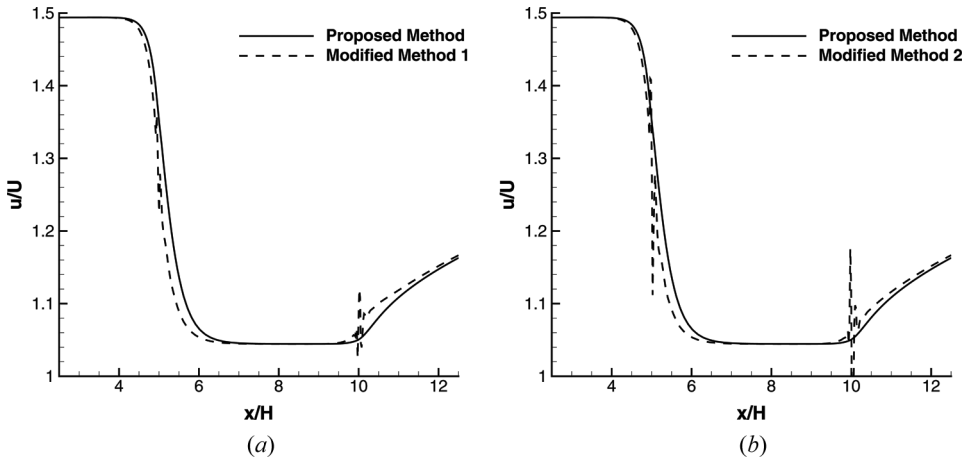


Figure 7. Plot of the streamwise velocity component for the porous plug problem at $\text{Re}_H = 1,000$ and $\text{Da} = 10^{-2}$ as a function of position along the line $y/H = 0.5$ on the interval $x/H \in [2.5, 12.5]$ for the modified methods of treating the interface pressure and gradients. Note that these cases were run using hexahedral grids.

faster than that of the second modified method. All cases were solved using a single large time step with a nonlinear residual tolerance, normalized by the average magnitude of the given field, specified as 10^{-6} . The proposed scheme converged in 43 iterations, while the two modified methods converged in 31 and 135 iterations, respectively. Thus, in addition to adding significant accuracy, the proposed method maintains good convergence properties.

Finally, we have computed results for $\text{Da} \in \{10^{-3}, 10^{-4}, 10^{-5}\}$ and $\text{Re}_H = 1,000$ to demonstrate the robustness of the model over a wide range of Darcy numbers with high Reynolds number. Results for the streamwise velocity component along the line $y/H = 0.5$ on the interval $x/H \in [2.5, 12.5]$ are plotted in Figure 8 and indicate that the model is capable of obtaining physically reasonable results for porous materials with low permeability.

5.2. Graphite Foam Heat Sink

Recently, there has been interest in creating graphite foam heat sinks with unique structures intended to balance the excellent heat transfer properties of graphite foam with its generally poor hydrodynamic properties, which lead to very high pressure losses when forcing fluid through the foam structure. Heat sinks proposed by Leong et al. [7] and Wu et al. [8] employ corrugated foam structures to allow fluid to pass relatively easily through the narrow porous regions while still obtaining some of its heat transfer benefits. The heat sink described in [8] is of particular relevance to this work because of its V-shaped corrugations, or “porous fins”, which cannot be discretized by orthogonal grids. With the present model, these heat sinks may be readily analyzed to determine their heat transfer characteristics and to perform optimization of their structure. While a complete parametric study is beyond the scope of this work, we shall demonstrate, using one particular flow configuration, the ability

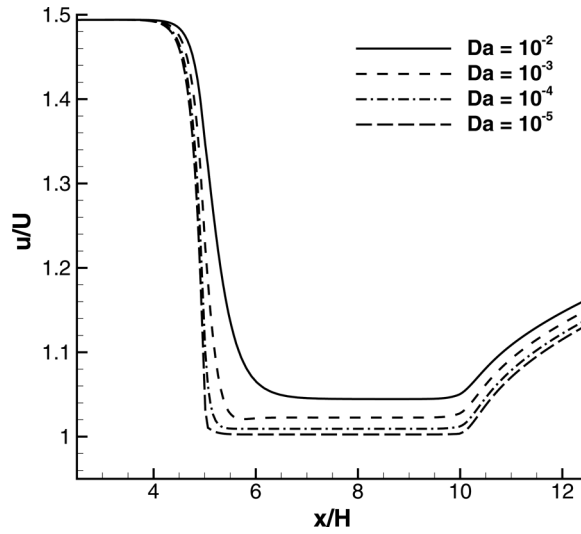


Figure 8. Plot of the streamwise velocity component for the porous plug problem at $Re_H = 1,000$ as a function of position along the line $y/H = 0.5$ on the interval $x/H \in [2.5, 12.5]$ for $Da \in \{10^{-2}, 10^{-3}, 10^{-4}, 10^{-5}\}$.

of the present model to solve the flow and thermal fields in such applications and show that the results are physically reasonable.

A schematic diagram of the geometry under consideration is given in Figure 9a. This geometry is a simplified version of the heat sink considered by Wu et al. [8], obtained by considering only one symmetric section of the heat sink and flattening the curved surfaces. Note that we have added fluid sections upstream and

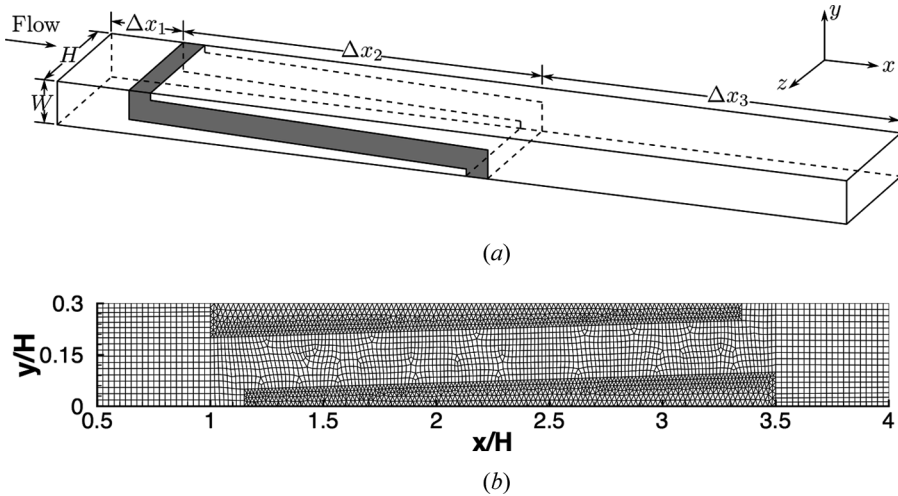


Figure 9. (a) Schematic diagram of the corrugated heat sink geometry, where the shaded region indicates the porous subdomain. (b) Plot of a selected portion of a 2-D section of the computational grid on a plane of constant z which uses both triangular prismatic and hexahedral volumes.

downstream of the heat sink in order to allow the fluid to enter and exit in a natural way. As in [8], the height of the heat sink was taken to be $H=20\text{mm}$. Additionally, we prescribed the dimensions $\Delta x_1/H=\Delta x_3/H=1$, $\Delta x_2/H=2.5$, and $W/H=0.3$. The thickness of the porous fins was taken to be $W/2$ and the slope of the fin was taken such that the fluid gap at the inlet of the heat sink was double the minimum gap size, occurring at $x/H=3.35$.

A uniform inflow condition was imposed at $x/H=0$ along with the mass-based outlet condition described in the previous section at $x/H=4.5$. On the upper and lower walls, $z/H=0$ and $z/H=1$, a no-slip condition was imposed, while on the symmetry planes, $y/W=0$ and $y/W=1$, zero-derivative conditions were applied. The pressure was set to a reference value of zero at the outlet and was extrapolated to all other nonsymmetric boundaries. On the symmetry planes, the derivative of pressure normal to the plane was set to zero. At the inlet and at the heated base, $x/H \in [1, 3.5]$, the uniform temperatures T_{in} and T_w were applied, respectively. At all remaining boundaries, adiabatic conditions were imposed. All graphite foam properties were taken from Straatman et al. [3] for POCO foam, and fluid properties were taken as standard properties of air.

A plot of a selected portion of the computational grid is given in Figure 9b, which shows the use of multiple volume types. Results for $\text{Re}_H=100$ are given in Figure 10 for the dimensionless pressure and temperature fields as well as some selected streamlines in the plane $z/H=0.5$. Based on the results for the dimensionless pressure, coupled with the plotted streamlines, we clearly see how the high pressure on one side of the porous region coupled with the low pressure on the other side leads to a fair amount of fluid being drawn directly through the foam. The dimensionless temperature plot clearly shows the rapid increase in temperature as the fluid picks up heat from the solid constituent of the graphite foam and exits the heat sink

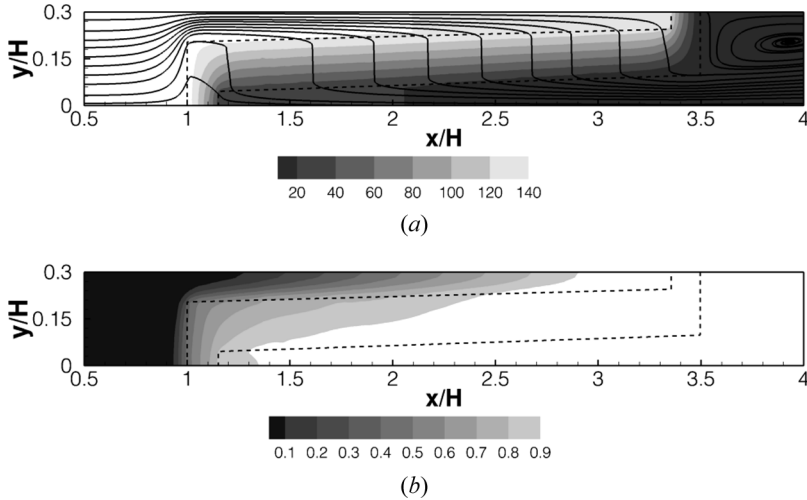


Figure 10. Contour plots on the plane $z/H=0.5$ of (a) the dimensionless pressure $\langle p \rangle^f / \rho_f U^2$ along with selected streamlines and (b) the dimensionless fluid temperature $(\langle T \rangle^f - T_{in}) / (T_w - T_{in})$. Note that the porous region is outlined with dashed lines.

at nearly the wall temperature. It should also be noted that although this grid is relatively coarse near interfaces, smooth results are still obtained.

The results given in this section are one example of a new class of problems that may now be solved numerically using the newly developed model for heat and fluid flow in conjugate fluid-porous domains. In this case, the geometry cannot be discretized using orthogonal grids, due to the sloped fins. The present model, however, is capable of obtaining physically reasonable results for this type of heat sink, although to compare directly with the experimental results of Wu et al. [8] a turbulence model would be required in the fluid regions, due to the higher Reynolds numbers considered in that work. Nevertheless, we have demonstrated that smooth results are obtained through the interface, and in future work more rigorous validation may be pursued for this and other cases.

6. CONCLUSIONS

A numerical model for computing fluid flow and heat transfer in conjugate fluid-porous domains using unstructured, nonorthogonal grids has been proposed. Novel, physically reasoned interface conditions have been proposed which are shown to be very robust at high laminar Reynolds numbers and induce no spurious oscillations in any of the solution fields. The major contribution of this model is the ability to use nonorthogonal grids to discretize complex geometries without affecting the robustness of the model or having any significant impact on the computational time required to obtain a solution.

REFERENCES

1. A. Bhattacharya and R. L. Mahajan, Finned Metal Foam Heat Sinks for Electronics Cooling in Forced Convection, *J. Electron. Packag.*, vol. 124, pp. 155–163, 2002.
2. K. Boomsma, D. Poulikakos, and F. Zwick, Metal Foams as Compact High Performance Heat Exchangers, *Mech. Mater.*, vol. 35, pp. 1161–1176, 2003.
3. A. G. Straatman, N. C. Gallego, Q. Yu, L. J. Betchen, and B. E. Thompson, Forced Convection and Hydraulic Losses in Graphitic Foam, *J. Heat Transf.—Transfer ASME*, vol. 129, pp. 1237–1245, 2007.
4. A. G. Straatman, N. C. Gallego, Q. Yu, and B. E. Thompson, Characterization of Porous Carbon Foam as a Material for Compact Recuperators, *J. Eng. Gas Turbines Power—Trans. ASME*, vol. 129, pp. 326–330, 2007.
5. L. J. Betchen and A. G. Straatman, The Development of a Volume-Averaged Entropy-Generation Function for Nonequilibrium Heat Transfer in High-Conductivity Porous Foams, *Numer. Heat Transfer B*, vol. 53, pp. 412–436, 2008.
6. C. T. DeGroot, A. G. Straatman, and L. J. Betchen, Modeling Forced Convection in Finned Metal Foam Heat Sinks, *J. Electron. Packag.*, vol. 131, 021001, 2009.
7. K. C. Leong, H. Y. Li, L. W. Jin, and J. C. Chai, Numerical and Experimental Study of Forced Convection in Graphite Foams of Different Configurations, *Appl. Thermal Eng.*, vol. 30, pp. 520–532, 2010.
8. W. Wu, J. H. Du, Y. R. Lin, L. C. Chow, H. Bostanci, B. A. Saarloos, and D. P. Rini, Evaluation of Compact, and Effective Air-Cooled Carbon Foam Heat Sink, *J. Heat Transfer—Trans. ASME*, vol. 133, 054504, 2011.

9. S. Whitaker, Diffusion and Dispersion in Porous Media, *AIChE J.*, vol. 13, pp. 420–427, 1967.
10. K. Vafai and C. L. Tien, Boundary and Inertia Effects on Flow and Heat Transfer in Porous Media, *Int. J. Heat Mass Transfer*, vol. 24, pp. 195–203, 1981.
11. Y. Ould-Amer, S. Chikh, K. Bouhadeh, and G. Lauriat, Forced Convection Cooling Enhancement by Use of Porous Materials, *Int. J. Heat Fluid Flow*, vol. 19, pp. 251–258, 1998.
12. S. Chikh, A. Boumedien, K. Bouhadeh, and G. Lauriat, Analysis of Fluid Flow and Heat Transfer in a Channel with Intermittent Heated Porous Blocks, *Heat Mass Transfer*, vol. 33, pp. 405–413, 1998.
13. W. S. Fu and S. F. Chen, A Numerical Study of Heat Transfer of a Porous Block with the Random Porosity Model in a Channel Flow, *Heat Mass Transfer*, vol. 38, pp. 695–704, 2002.
14. M. S. Phanikumar and R. L. Mahajan, Non-Darcy Natural Convection in High Porosity Metal Foams, *Int. J. Heat Mass Transfer*, vol. 45, pp. 3781–3793, 2002.
15. V. V. Calmidi and R. L. Mahajan, Forced Convection in High Porosity Metal Foams, *J. Heat Transfer—Trans. ASME*, vol. 122, pp. 557–565, 2000.
16. V. A. F. Costa, L. A. Oliveira, B. R. Baliga, and A. C. M. Sousa, Simulation of Coupled Flows in Adjacent Porous and Open Domains Using a Control-Volume Finite-Element Method, *Numer. Heat Transfer A*, vol. 45, pp. 675–697, 2004.
17. V. A. F. Costa, L. A. Oliveira, and B. R. Baliga, Implementation of the Stress Jump Condition in a Control-Volume Finite-Element Method for the Simulation of Laminar Coupled Flows in Adjacent Open and Porous Domains, *Numer. Heat Transfer B*, vol. 53, pp. 383–411, 2008.
18. L. J. Betchen, A. G. Straatman, and B. E. Thompson, A Nonequilibrium Finite-Volume Model for Conjugate Fluid/Porous/Solid Domains, *Numer. Heat Transfer A*, vol. 49, pp. 543–565, 2006.
19. P. Yu, T. S. Lee, Y. Zeng, and H. T. Low, A Numerical Method for Flows in Porous and Homogeneous Fluid Domains Coupled at the Interface by Stress Jump, *Int. J. Numer. Meth. Fluids*, vol. 53, pp. 1755–1775, 2007.
20. S. Whitaker, Volume Averaging of Transport Equation, in J. P. Du Plessis (ed.), *Fluid Transport in Porous Media*, chap. 1, Springer-Verlag, Southampton, UK, 1997.
21. A. Amiri, K. Vafai, and T. M. Kuzay, Effects of Boundary Conditions on Non-Darcian Heat Transfer through Porous Media and Experimental Comparisons, *Numer. Heat Transfer A*, vol. 27, pp. 651–664, 1995.
22. M. L. Martins-Costa and R. M. S da Gama, A Local Model for the Heat Transfer Process in Two Distinct Flow Regions, *Int. J. Heat Fluid Flow*, vol. 15, pp. 477–485, 1994.
23. K. Vafai and S. J. Kim, On the Limitations of the Brinkman-Forchheimer-Extended Darcy Equation, *Int. J. Heat Fluid Flow*, vol. 16, pp. 11–15, 1995.
24. J. A. Ochoa-Tapia and S. Whitaker, Momentum Transfer at the Boundary between a Porous Medium and a Homogeneous Fluid—I. Theoretical Development, *Int. J. Heat Mass Transfer*, vol. 38, pp. 2635–2646, 1995.
25. B. Alazmi and K. Vafai, Analysis of Fluid Flow and Heat Transfer Interfacial Conditions Between a Porous Medium and a Fluid Layer, *Int. J. Heat Mass Transfer*, vol. 44, pp. 1735–1749, 2002.
26. L. J. Betchen and A. G. Straatman, An Accurate Gradient and Hessian Reconstruction Method for Cell-Centered Finite Volume Discretizations on General Unstructured Grids, *Int. J. Numer. Meth. Fluids*, vol. 62, pp. 945–962, 2010.
27. V. Venkatakrishnan, Convergence to Steady-State Solutions of the Euler Equations on Unstructured Grids with Limiters, *J. Comput. Phys.*, vol. 118, no. 1, pp. 120–130, 1995.

28. A. Dalal, V. Eswaran, and G. Biswas, A Finite-Volume Method for Navier-Stokes Equations on Unstructured Grids, *Numer. Heat Transfer B*, vol. 54, pp. 238–259, 2008.
29. I. Demirdžić, and S. Muzaferija, Numerical Method for Coupled Fluid Flow, Heat Transfer and Stress Analysis Using Unstructured Moving Meshes with Cells of Arbitrary Topology, *Comput. Meth. Appl. Mech. Eng.*, vol. 125, pp. 235–255, 1995.
30. C. M. Rhie and W. L. Chow, Numerical Study of the Turbulent Flow Past an Airfoil with Trailing Edge Separation, *AIAA J.*, vol. 21, pp. 1525–1532, 1983.
31. M. Moradi Larmaei, J. Behzadi, and T.-F. Mahdi, Treatment of Checkerboard Pressure in the Collocated Unstructured Finite-Volume Scheme, *Numer. Heat Transfer B*, vol. 58, pp. 121–144, 2010.